

## Electronic Supplementary Information

### **Integrating Molecular Rigidity and Chirality into Thermally Activated Delayed Fluorescence Emitters for Highly Efficient Sky-blue and Orange Circularly Polarized Electroluminescence**

*Fan Ni,<sup>[ab]</sup> Chih-Wei Huang,<sup>[c]</sup> Yukun Tang,<sup>[c]</sup> Zhanxiang Chen,<sup>[d]</sup> Yaxun Wu,<sup>[d]</sup> Shengpeng*

*Xia,<sup>[d]</sup> Xiaosong Cao,<sup>[a]</sup> Jung-Hsien Hsu,<sup>[c]</sup> Wei-Kai Lee,<sup>[c]</sup> Kailu Zheng,<sup>[d]</sup> Zhongyan*

*Huang,<sup>[a]</sup> Chung-Chih Wu,<sup>\*[c]</sup> and Chuluo Yang<sup>\*[a]</sup>*

<sup>[a]</sup> Shenzhen Key Laboratory of Polymer Science and Technology, College of Materials Science and Engineering, Shenzhen University, Shenzhen, 518060, P. R. China. E-mail: [clyang@szu.edu.cn](mailto:clyang@szu.edu.cn)

<sup>[b]</sup> Key Laboratory of Optoelectronic Devices and Systems of Ministry of Education and Guangdong Province, College of Optoelectronic Engineering, Shenzhen University, Shenzhen 518060, China.

<sup>[c]</sup> Department of Electrical Engineering, Graduate Institute of Electronics Engineering and Graduate Institute of Photonics and Optoelectronics, National Taiwan University, Taipei, 10617, Taiwan. E-mail: [wucc@ntu.edu.tw](mailto:wucc@ntu.edu.tw)

<sup>[d]</sup> Department of Chemistry and Hubei Key Lab on Organic and Polymeric Optoelectronic Materials, Wuhan University, Wuhan, 430072, P. R. China.

F. Ni and C. W. Huang contributed equally to this work.

## Table of contents

1. General information.....	3
2. Devices fabrication and characterization .....	9
3. Synthesis of TRZ-MeIAc and NID-MeIAc.....	10
4. The report of the chiral HPLC resolution.....	12
5. X-ray single crystal structure analysis .....	14
6. Thermal and electrochemical properties.....	16
7. Photophysical properties.....	18
8. Theoretical simulation .....	21
9. The analysis of the absolute configuration .....	24
10. Supplemental electroluminescence data .....	25
11. <sup>1</sup> H NMR, <sup>13</sup> C NMR and HRMS spectroscopies .....	34
12. References .....	37

## 1. General information

Commercially available reagents were used as received without further purification. Toluene and tetrahydrofuran (THF) were dried by sodium-potassium alloy, *N,N*-dimethylacetamide (DMA) was dried by calcium hydride ( $\text{CaH}_2$ ).  $^1\text{H}$  NMR and  $^{13}\text{C}$  NMR spectra were recorded on a Bruker Advanced II (400 MHz) spectrometers.  $^1\text{H}$  and  $^{13}\text{C}$  NMR chemical shifts were reported in parts per million (ppm) relative to  $\text{Me}_4\text{Si}$  as an external standard. High-resolution mass spectra were measured on a Bruker Compact TOF mass spectrometer or a Thermo Scientific Quadrupole-Orbitrap Mass Spectrometer in electrospray ionization mode (ESI<sup>+</sup>). Differential scanning calorimetry (DSC) was performed on a NETZSCH DSC 200 PC unit at a heating rate of  $10\text{ }^\circ\text{C min}^{-1}$  from 20 to  $300\text{ }^\circ\text{C}$  under argon. The glass transition temperature ( $T_g$ ) was determined from the second heating scan. Thermogravimetric analysis (TGA) was undertaken with a Perkin Elmer Pyris instrument. The thermal stability of the samples under the nitrogen atmosphere was determined by measuring their weight loss while heating at a rate of  $10\text{ }^\circ\text{C min}^{-1}$  from 25 to  $600\text{ }^\circ\text{C}$ . The temperature of degradation ( $T_d$ ) was correlated to a 5% weight loss. Cyclic voltammetry (CV) was carried out in dichloromethane at room temperature with a CHI voltammetric analyzer. Tetrabutylammonium hexafluorophosphate ( $\text{TBAPF}_6$ ) (0.1 M) was used as the supporting electrolyte. The conventional three-electrode configuration consists of a platinum working electrode, a platinum wire auxiliary electrode, and an Ag wire pseudo-reference electrode with ferrocenium-ferrocene ( $\text{Fc}^+/\text{Fc}$ ) as the internal standard. Formal potentials are calculated as the average of cyclic voltammetric peaks. UV-vis absorption spectra were recorded on a Shimadzu UV-2700 recording spectrophotometer. Fluorescence and phosphorescence emission spectra at room temperature or 77 K were measured on a Hitachi F-4600 spectrophotometer.  $E_S$  and  $E_T$  were calculated from the onset of the fluorescence spectra and the phosphorescence spectra, respectively. The transient photoluminescence decay curves were measured on an Edinburgh FLS920 spectrophotometer. Absolute PLQYs were obtained using a Quantaaurus-QY measurement system (C11347-11, Hamamatsu Photonics). The circular dichroism (CD) were measured on Chirascan<sup>TM</sup> circular dichroic spectropolarimeter. The circularly polarized luminescence (CPPL and CPEL) spectra were measured on Jasco CPL-300 spectrometer. The test mode adopts “Slit” mode with the  $E_x$  and  $E_m$  Slit width  $3000\text{ }\mu\text{m}$  and the digital integration time (D.I.T.) is 2.0 s with multiple accumulations. Single-crystal X-ray-diffraction data for **TRZ-MeIAc** were collected on Rigaku Oxford Diffraction Supernova Dual Source, Cu at Zero equipped with an AtlasS2 CCD using  $\text{CuK}\alpha$  radiation. The ground state molecular structures were optimized at the B3LYP-D3(BJ)/def2-SVP level of theory.<sup>1</sup> The flexible potential surface scanning on the energy of the ground state geometry at different

twisted angles was based on B3LYP/def2-SVP level of theory. Energy gaps between the S<sub>1</sub> and T<sub>1</sub> states were calculated using the PBE0/def2-SVP theory.<sup>2</sup> The configuration of the S<sub>1</sub> state was calculated at the CAM-B3LYP/def2-SVP level. The flexible potential surface scanning on the energy of the excited singlet state geometry at different twisted angles was based on CAM-B3LYP/def2-SVP level of theory. The RMSD values between S<sub>0</sub> and S<sub>1</sub> states were obtained through Multiwfn.<sup>2</sup> The oscillator strength ( $f$ ) was calculated through the nuclear ensemble approach.<sup>3</sup> The rotational strength R, electric ( $\vec{\mu}$ ) and magnetic ( $\vec{m}$ ) transition dipole moments and their vector angles ( $\theta_{\mu,m}$  in degrees) were calculated at the PBE0/def2-SVP level with the toluene solvent correction.<sup>4</sup>

The single-crystal of (*R*)-TRZ-MeIAc (CCDC number: 1971785) was obtained from the solvent diffusion method from *n*-hexane/chloroform mixed solutions.

The rate equation for singlet and triplet exciton ( $S_1$  and  $T_1$ ) is described by

$$\frac{d}{dt} \begin{pmatrix} S_1 \\ T_1 \end{pmatrix} = \begin{pmatrix} -(k_{r,S} + k_{nr,S} + k_{ISC}) & +k_{RISC} \\ k_{ISC} & -(k_{r,T} + k_{nr,T} + k_{RISC}) \end{pmatrix} \begin{pmatrix} S_1 \\ T_1 \end{pmatrix}$$

where  $k_{r,S}$ ,  $k_{nr,S}$  and  $k_{ISC}$  are the rate constants of radiative decay (fluorescence), intrinsic non-radiative decay (internal conversion) and ISC for singlet excitons, respectively.  $k_{r,T}$ ,  $k_{nr,T}$  and  $k_{RISC}$  are the rate constants of radiative decay (phosphorescence), intrinsic non-radiative decay and RISC of the triplet exciton, respectively.<sup>5</sup>

$k_p$ ,  $k_d$ ,  $k_{r,S}$ ,  $k_{RISC}$ ,  $k_{ISC}$  and  $k_{IC}^S$  can be obtained:

$$k_p = \frac{1}{\tau_p} \quad \text{Eq. S1}$$

$$k_d = \frac{1}{\tau_d} \quad \text{Eq. S2}$$

$$k_{r,s} = k_p \Phi_p + k_d \Phi_d \approx k_p \Phi_p \quad \text{Eq. S3}$$

$$k_{RISC} \approx \frac{k_p k_d \Phi}{k_{r,s}} = \frac{\Phi}{\tau_d \Phi_p} \quad \text{Eq. S4}$$

$$k_{ISC} \approx \frac{k_p k_d \Phi_d}{k_{RISC} \Phi_p} = \frac{\Phi_d}{\tau_p \Phi} \quad \text{Eq. S5}$$

$$k_{IC}^S \approx \frac{1-\Phi}{\Phi \tau_p} \Phi_p \quad \text{Eq. S6}$$

The prompt PLQY ( $\Phi_p$ ) and delayed PLQY ( $\Phi_d$ ) were determined by using the total PLQY ( $\Phi$ ) and the integrated intensity ratio between prompt and delayed components which was calculated from transient photoluminescence measurements. The intensity ratios between prompt ( $r_p$ ) and delayed ( $r_d$ ) components were determined using two fluorescent lifetimes ( $\tau_p$ ,  $\tau_d$ ) and fitting parameter ( $A_p$ ,  $A_d$ ) as follow.

$$I(t) = A_p e^{-\frac{t}{\tau_p}} + A_d e^{-\frac{t}{\tau_d}} \quad \text{Eq. S7}$$

$$r_p = \frac{A_p \tau_p}{A_p \tau_p + A_d \tau_d} \quad \text{Eq. S8}$$

$$r_d = \frac{A_d \tau_d}{A_p \tau_p + A_d \tau_d} \quad \text{Eq. S9}$$

Then, the prompt PLQY ( $\Phi_p$ ) and delayed PLQY ( $\Phi_d$ ) were determined using intensity ratio ( $r_p$ ,  $r_d$ ) and total PLQY ( $\Phi$ ).

$$\Phi = \Phi_p + \Phi_d \quad \text{Eq. S10}$$

$$\Phi_p = r_p \Phi \quad \text{Eq. S11}$$

$$\Phi_d = r_d \Phi \quad \text{Eq. S12}$$

The luminescence dissymmetry ratio can be related to the molecular transition matrix elements as follows<sup>6</sup>:

$$g_{\text{lum}} = \frac{\Delta I}{\frac{1}{2}I} = \frac{I_L - I_R}{\frac{1}{2}(I_L + I_R)} = -4i \frac{\mu_1^{gn} m_1^{gn} + \mu_2^{gn} m_2^{gn}}{|\mu_1^{gn}|^2 + |\mu_2^{gn}|^2 + |m_1^{gn}|^2 + |m_2^{gn}|^2} \quad \text{Eq. S13}$$

where  $I_L$  and  $I_R$  are the intensity of left- and right-circularly polarized light,  $\Delta I$  is the the intensity of left-circularly polarized light ( $I_L$ ) versus right-circularly polarized light ( $I_R$ ),  $I$  is the total luminescence intensity. 1 and 2 refer to laboratory axes,  $\mu_1^{gn}$  and  $\mu_2^{gn}$  are the electric transition dipole moment of the two axes respectively and  $m_1^{gn}$  and  $m_2^{gn}$  are the magnetic transition dipole moment of the two axes, respectively.

We can make the simplifying assumptions that the lineshapes for CPL and total luminescence are identical and that the number of molecules in the emitting state is independent of their orientation. The direct connection to molecular structure relies on relating the transition matrix elements from laboratory to molecular coordinate systems. For the case of a randomly oriented emitting distribution, the orientational averaging yields the following general result:

$$g_{\text{lum}} = 4\text{Re} \left[ \frac{\vec{\mu}^{gn} \cdot \vec{m}^{gn}}{|\vec{\mu}^{gn}|^2 + |\vec{m}^{gn}|^2} \right] = 4\text{Re} \left[ \frac{|\vec{\mu}^{gn}| \cdot |\vec{m}^{gn}| \cdot \cos \theta_{\mu,m}}{|\vec{\mu}^{gn}|^2 + |\vec{m}^{gn}|^2} \right] \quad \text{Eq. S14}$$

where  $\vec{\mu}^{gn}$ ,  $\vec{m}^{gn}$  are the electric and magnetic transition dipole moments, respectively.  $\theta_{\mu,m}$  is the vector angle between  $\vec{\mu}^{gn}$  and  $\vec{m}^{gn}$ .

Usually, the value of magnetic transition dipole moments ( $|\vec{m}^{gn}|$ ) are typically smaller than the value of electric transition dipole moments ( $|\vec{\mu}^{gn}|$ ) in pure organic systems, so that the value of  $|\vec{m}^{gn}|^2$  is much smaller than that of  $|\vec{\mu}^{gn}|^2$ . The Eq. S14 can be further simplified as follows:

$$g_{\text{lum}} = 4\text{Re} \left[ \frac{\vec{\mu}^{gn} \cdot \vec{m}^{gn}}{|\vec{\mu}^{gn}|^2 + |\vec{m}^{gn}|^2} \right] \approx 4\text{Re} \left[ \frac{|\vec{\mu}^{gn}| \cdot |\vec{m}^{gn}| \cdot \cos \theta_{\mu,m}}{|\vec{\mu}^{gn}|^2} \right] = 4\text{Re} \left[ \frac{|\vec{m}^{gn}| \cdot \cos \theta_{\mu,m}}{|\vec{\mu}^{gn}|} \right] \quad \text{Eq. S15}$$

Oscillator strength ( $f$ ) is a very important physical quantity during the electronic excitation process. The oscillator strength characterizes the strength of the electron excitation. The oscillator strength of the  $i$ th excited state is mainly related to the transition dipole moment and is defined as:<sup>7</sup>

$$f_i = \frac{2m_e}{3\hbar^2 e^2} E_i (D_{ix}^2 + D_{iy}^2 + D_{iz}^2) = \frac{2m_e}{3\hbar^2 e^2} E_i |\vec{\mu}_i|^2 \quad \text{Eq. S16}$$

where  $m_e$  is the mass of an electron,  $\hbar$  is the reduced Planck's constant,  $e$  is the charge of electron,  $D_{ix}$ ,  $D_{iy}$ , and  $D_{iz}$  are the electric transition dipole moments of different components, respectively;  $E_i$  is the excitation energy of the  $i$ th excited state;  $\vec{\mu}_i$  is the electric dipole moment from the ground state to the  $i$ th excited state.

The oscillator strength of the lowest excited singlet state is defined as:

$$f = \frac{2m_e}{3\hbar^2 e^2} E_{S1} (D_{1x}^2 + D_{1y}^2 + D_{1z}^2) = \frac{2m_e}{3\hbar^2 e^2} E_{S1} |\vec{\mu}|^2 \quad \text{Eq. S17}$$

where  $D_{1x}$ ,  $D_{1y}$ , and  $D_{1z}$  are the electric transition dipole moments of different components at the lowest excited singlet state, respectively;  $E_{S1}$  is the lowest excited singlet state energy;  $\vec{\mu}$  is the electric dipole moment from the ground state to the lowest excited singlet state.



## 2. Devices fabrication and characterization

All organic materials used in experiments (except for the TADF emitters) were purchased from Lumtec, Inc. All compounds were subjected to temperature-gradient sublimation under a high vacuum before use. OLEDs were fabricated on the ITO-coated glass substrates with multiple organic layers sandwiched between the transparent bottom indium-tin-oxide (ITO) anode and the top metal cathode. All material layers were deposited by vacuum evaporation in a vacuum chamber with a base pressure of  $10^{-6}$  torr. The deposition system permits the fabrication of the complete device structure in a single vacuum pump-down without breaking vacuum. The deposition rate of organic layers was kept at 0.1 - 0.2 nm/s. The doping was conducted by co-evaporation from separate evaporation sources with different evaporation rates. The active area of the device is  $1 \times 1 \text{ mm}^2$ , as defined by the 10 shadow mask for cathode deposition. The current-voltage-brightness (J-V-L) characterization of the light-emitting devices was performed with a source-measurement unit (SMU) and a spectroradiometer (DMS 201, AUTRONIC-MELCHERS GmbH). EL spectra of devices were collected by a calibrated CCD spectrograph. The angular dependence of EL intensities (and spectra) was measured by a calibrated goniometric spectroradiometer (DMS 201, AUTRONIC-MELCHERS GmbH). The external quantum efficiencies of devices were determined by collecting the total emission fluxes with a calibrated integrating-sphere measurement system and by measuring the angular distribution of the emission spectra and intensities.

### 3. Synthesis of TRZ-MeIAc and NID-MeIAc

#### 3.1 The synthesis of 5-(4-(4,6-diphenyl-1,3,5-triazin-2-yl)phenyl)-12b-methyl-5,12b-dihydroindeno[1,2,3-*kl*]acridine (TRZ-MeIAc)

2-(2-bromophenyl)-4,6-diphenyl-1,3,5-triazine (1.55 g, 4.0 mmol), MeIAc (1.19 g, 4.4 mmol), palladium(II) acetate (18 mg, 0.08 mmol), tri-*tert*-butylphosphine tetrafluoroborate (70 mg, 0.24 mmol) and sodium *tert*-butoxide (422 mg, 4.4 mmol) were added to dry toluene (20 mL). The mixture was stirred at reflux for 24 hours and then cooled to room temperature. The reaction mixture was slowly poured into water and extracted with CH<sub>2</sub>Cl<sub>2</sub> (100 mL ×3). The organic phase was dried over anhydrous Na<sub>2</sub>SO<sub>4</sub>, filtered and concentrated under reduced pressure. The crude product was purified by column chromatography with petroleum ether/CH<sub>2</sub>Cl<sub>2</sub> (*v/v* = 1/1) as eluent, finally the light yellow powder TRZ-MeIAc was obtained with a yield of 82%. The resulting product was further purified by recrystallizing from a mixture of CHCl<sub>3</sub>/hexane to give light yellow crystal. The obtained compound was further purified by vacuum sublimation (with pressure less than 10<sup>-5</sup> Pa) at 240 °C with a yield of 83%. <sup>1</sup>H NMR (400 MHz, CD<sub>2</sub>Cl<sub>2</sub>, δ): 9.03 (d, *J* = 8.4 Hz, 2H), 8.81 (d, *J* = 8.0 Hz, 4H), 8.03 (d, *J* = 7.6 Hz, 1H), 7.85 (t, *J* = 6.8 Hz, 2H), 7.58-7.68 (m, 8H), 7.43-7.49 (m, 3H), 7.23 (t, *J* = 7.6 Hz, 1H), 7.07 (t, *J* = 5.6 Hz, 2H), 6.70 (d, *J* = 8.0 Hz, 1H), 6.60 (d, *J* = 8.0 Hz, 1H), 1.51 (s, 3H); <sup>13</sup>C NMR (100 MHz, CD<sub>2</sub>Cl<sub>2</sub>, δ): 172.3, 171.6, 150.9, 145.3, 143.7, 141.3, 140.6, 138.4, 136.7, 136.4, 134.5, 133.3, 131.7, 131.0, 129.5, 129.3, 128.5, 128.0, 127.9, 127.8, 126.9, 126.3, 125.1, 122.6, 121.9, 116.3, 114.0, 112.8, 48.4, 23.0. HRMS (ESI, *m/z*): [M+H]<sup>+</sup> calcd for C<sub>41</sub>H<sub>29</sub>N<sub>4</sub><sup>+</sup>: 577.2387; found: 577.2390. Anal. calcd for C<sub>41</sub>H<sub>28</sub>N<sub>4</sub>: C, 85.39; H, 4.89; N, 9.72; found: C, 85.13; H, 5.07; N, 9.80.

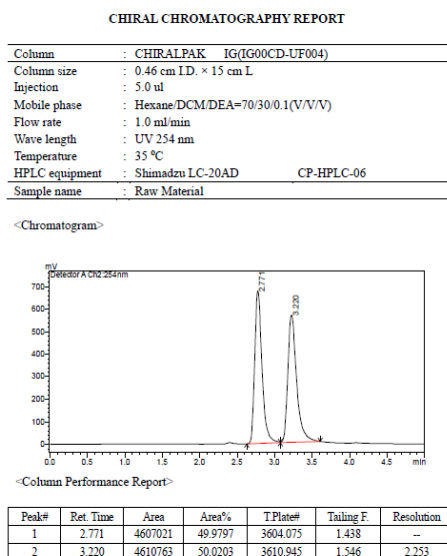
### 3.2 The synthesis of 2-(4-(tert-butyl)phenyl)-6-(12b-methylindeno[1,2,3-*k*]acridin-5(12bH)-yl)-1H-benzo[*de*]isoquinoline-1,3(2H)-dione (NID-MeIAc)

4-bromo-9-(4-tert-butylphenyl)-1,8-naphthalimide (1.63 g, 4.0 mmol), MeIAc (1.19 g, 4.4 mmol), palladium(II) acetate (18 mg, 0.08 mmol), tri-tert-butylphosphine tetrafluoroborate (70 mg, 0.24 mmol) and sodium tert-butoxide (422 mg, 4.4 mmol) were added to dry toluene (20 mL). The mixture was stirred at reflux for 24 hours then cooled to room temperature. The reaction mixture was slowly poured into water and extracted with CH<sub>2</sub>Cl<sub>2</sub> (100 mL ×3). The organic phase was dried over anhydrous Na<sub>2</sub>SO<sub>4</sub>, filtered and concentrated under reduced pressure. The crude product was purified by column chromatography with petroleum ether/CH<sub>2</sub>Cl<sub>2</sub> (*v/v* = 3/1) as eluent, finally the orange-red powder NID-MeIAc was obtained with a yield of 76%. The resulting product was further purified by recrystallizing from a mixture of CHCl<sub>3</sub>/EtOH to give orange-red powder. The obtained compound was further purified by vacuum sublimation (with pressure less than 10<sup>-5</sup> Pa) at 275 °C with a yield of 91%. <sup>1</sup>H NMR (400 MHz, CD<sub>2</sub>Cl<sub>2</sub>, δ): 8.85 (d, *J* = 7.6 Hz, 1H), 8.59-8.65 (m, 2H), 8.09 (d, *J* = 6.0 Hz, 1H), 7.88-7.96 (m, 3H), 7.62-7.76 (m, 3H), 7.46-7.54 (m, 3H), 7.30 (d, *J* = 8.4 Hz, 2H), 6.99-7.15 (m, 3H), 6.02-6.43 (m, 2H), 1.59-1.65 (m, 3H), 1.43 (s, 9H); <sup>13</sup>C NMR (100 MHz, CD<sub>2</sub>Cl<sub>2</sub>, δ): 164.6, 164.3, 152.3, 150.9, 143.8, 143.4, 141.0, 138.6, 133.9, 133.5, 132.6, 131.6, 131.0, 130.2, 129.1, 128.8, 128.7, 128.4, 128.1, 128.0, 127.3, 127.1, 126.9, 126.6, 126.5, 126.3, 125.4, 124.4, 123.7, 123.0, 122.0, 115.7, 114.4, 112.1, 48.3, 35.3, 31.7, 31.2. HRMS (ESI, *m/z*): [M+Na]<sup>+</sup> calcd for C<sub>42</sub>H<sub>32</sub>N<sub>2</sub>NaO<sub>2</sub><sup>+</sup>: 619.2356; found: 619.2361. Anal. calcd for C<sub>42</sub>H<sub>32</sub>N<sub>2</sub>O<sub>2</sub>: C, 84.54; H, 5.41; N, 4.69; found: C, 84.78; H, 5.13; N, 4.73.

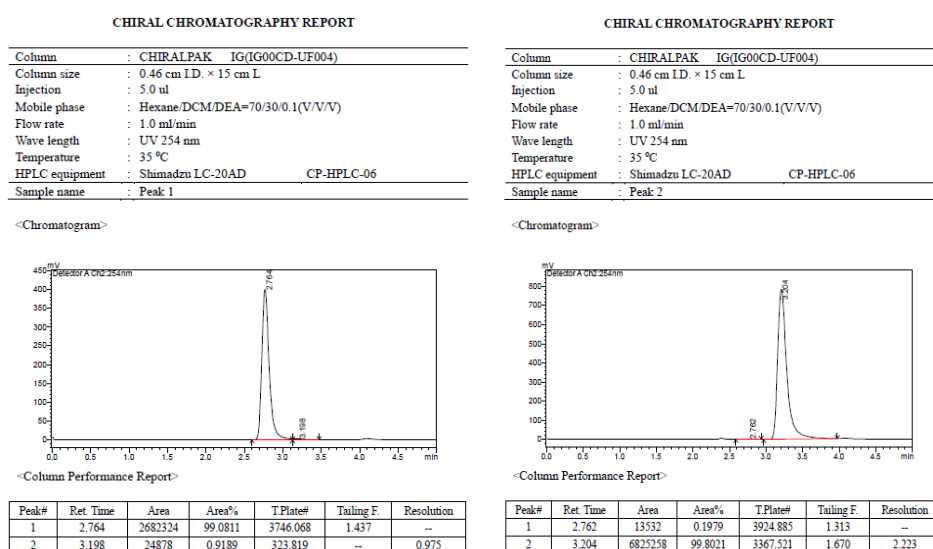
## 4. The report of the chiral HPLC resolution

The resolution of the enantiomers of TRZ-MeIac and NID-MeIac was conducted through chiral high-performance liquid chromatography column by DAICEL Chiral Technologies (CHINA) CO., LTD. The enantiomeric excess (e.e.) values for the two pairs of enantiomers are all above 98%.

### 4.1 The report of the chiral HPLC resolution of TRZ-MeIac

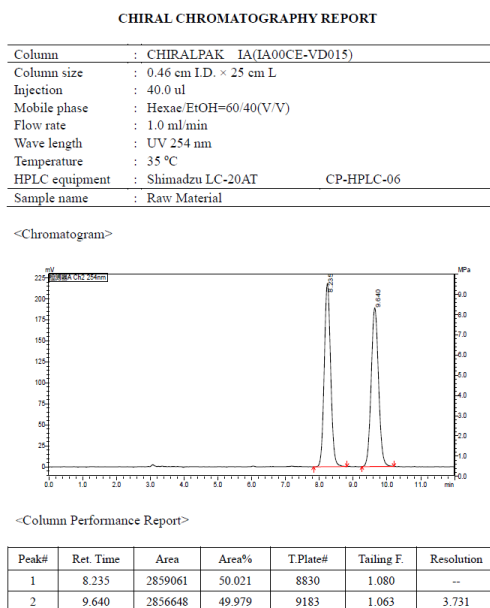


**Figure S1.** The report of the chiral HPLC resolution of TRZ-MeIac.

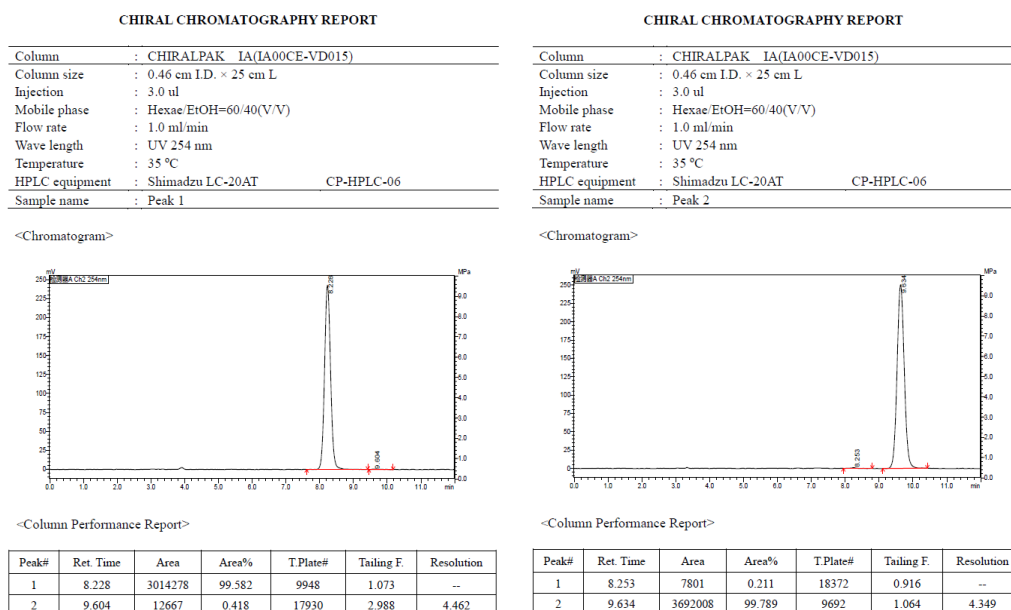


**Figure S2.** The report of the chiral HPLC resolution of (*R*)-TRZ-MeIac (Peak 1) and (*S*)-TRZ-MeIac (Peak 2).

## 4.2 The report of the chiral HPLC resolution of NID-MeIAC



**Figure S3.** The report of the chiral HPLC resolution of NID-MeIAC.

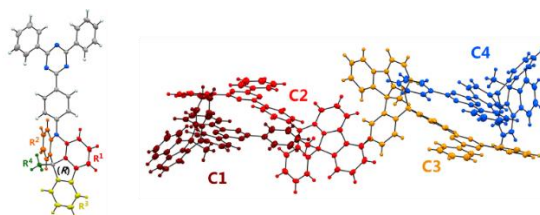


**Figure S4.** The report of the chiral HPLC resolution of (*R*)-NID-MeIAC (Peak 1) and (*S*)-NID-MeIAC (Peak 2).

## 5. X-ray single crystal structure analysis

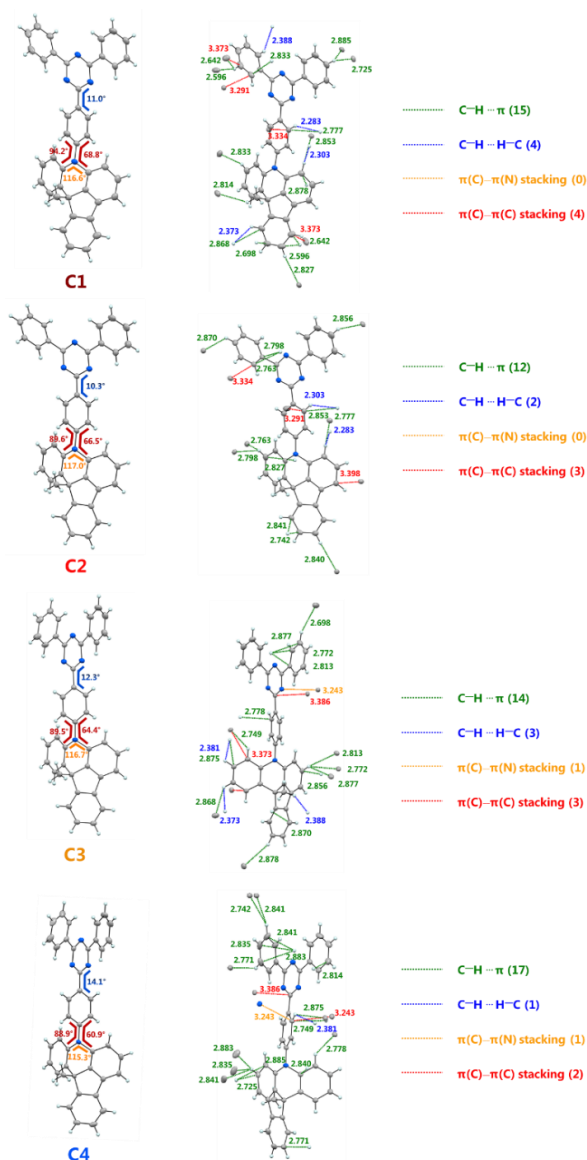
**Table S1.** Single crystal data and structure refinement of (*R*)-TRZ-MeIAc

Compound name	( <i>R</i> )-TRZ-MeIAc
Empirical formula	C <sub>41</sub> H <sub>28</sub> N <sub>4</sub>
Formula weight	576.67
Temperature/K	100.00(10)
Crystal system	monoclinic
Space group	P2 <sub>1</sub>
a/Å	17.0490(3)
b/Å	14.1638(2)
c/Å	25.7784(4)
α/°	90
β/°	103.8957(18)
γ/°	90
Volume/Å <sup>3</sup>	6042.75(18)
Z	8
ρ <sub>calc</sub> /cm <sup>3</sup>	1.268
μ/mm <sup>-1</sup>	0.582
F(000)	2416.0
Crystal size/mm <sup>3</sup>	0.12 × 0.1 × 0.08
Radiation	CuKα (λ = 1.54184)
2Θ range for data collection/°	5.34 to 147.964
Index ranges	-21 ≤ h ≤ 19, -17 ≤ k ≤ 16, -31 ≤ l ≤ 31
Reflections collected	41719
Independent reflections	22475 [R <sub>int</sub> = 0.0355, R <sub>sigma</sub> = 0.0509]
Data/restraints/parameters	22475/1/1625
Goodness-of-fit on F <sup>2</sup>	1.017
Final R indexes [I > 2σ (I)]	R <sub>1</sub> = 0.0418, wR <sub>2</sub> = 0.0948
Final R indexes [all data]	R <sub>1</sub> = 0.0519, wR <sub>2</sub> = 0.1010
Largest diff. peak/hole / e <sup>-</sup> Å <sup>-3</sup>	0.14/-0.18
Flack parameter	0.1(2)



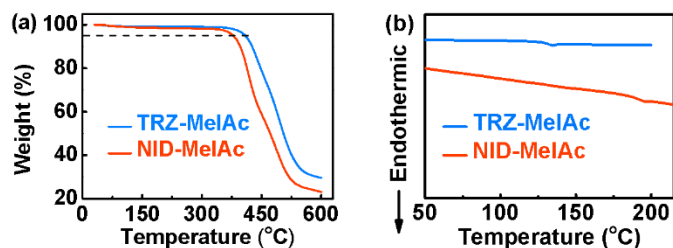
**Figure S5.** X-ray structural details of (*R*)-TRZ-MeIAc (CCDC number 1971785).

The absolute configuration-related Flack parameter of the single crystal is 0.1(2) (Table S1), suggesting the absolute configuration can be confirmed<sup>9</sup> and turns out to be *R*.



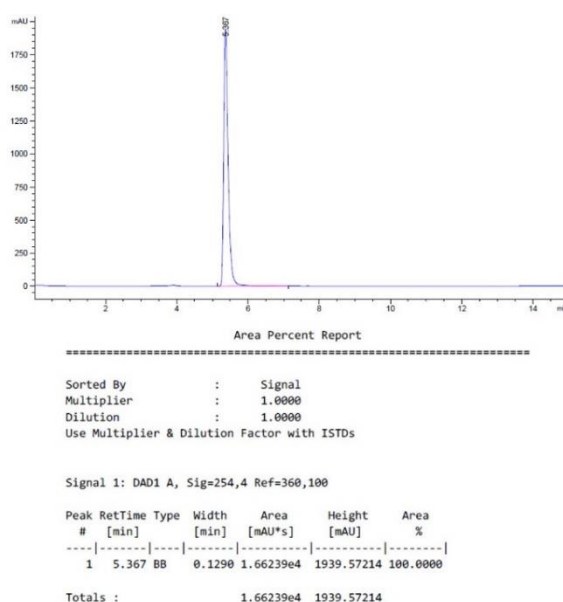
**Figure S6.** The packing model of (*R*)-TRZ-MeIAc in single crystal structure, blue ball for nitrogen, grey ball for carbon, white ball for hydrogen.

## 6. Thermal and electrochemical properties



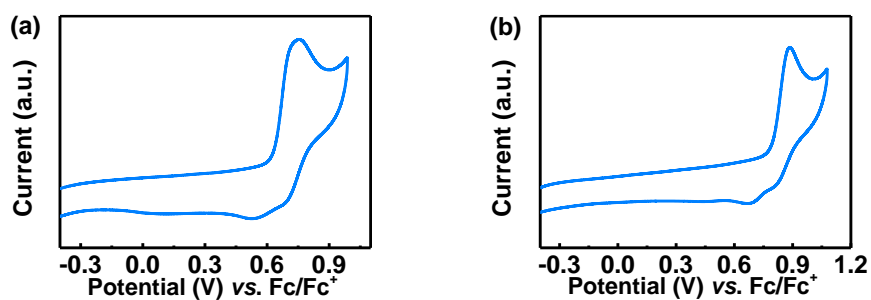
**Figure S7.** (a) Thermogravimetric analysis (TGA) curves and (b) differential scanning calorimeter (DSC) curves of TRZ-MeIAC and NID-MeIAC.

The racemization of chiral carbon-based molecules is difficult as a function of bond cleavage at the stereogenic center should be present.<sup>10</sup> The chiral carbon in MeIAC is fixed with the three linked aryl substituents forming a rigid connection with each other. The fixed structure in MeIAC means that the thermal racemization would be hard. As to evaluate the chirality stability of CPTADF emitters, the chiral HPLC analysis of (*R*)-TRZ-MeIAC after vacuum sublimation at 240 °C for 2 days was conducted. The report shows that no racemization occurs, confirming the thermal stability (**Figure S8**).



**Figure S8.** The report of the chiral HPLC analysis of (*R*)-TRZ-MeIAC after vacuum sublimation at 240 °C.





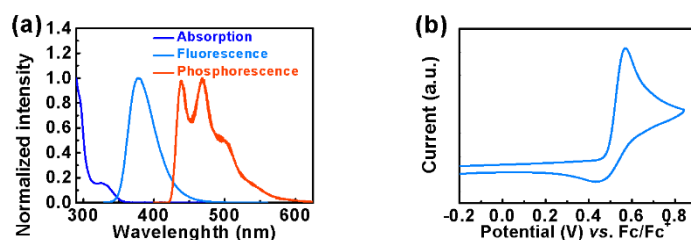
**Figure S9.** Cyclic voltammograms of TRZ-MeIAc (a) and NID-MeIAc (b) in CH<sub>2</sub>Cl<sub>2</sub>.

**Table S2.** Thermal and electrochemical properties of TRZ-MeIAc and NID-MeIAc.

Compound	$T_d^a$ [°C]	$T_g^b$ [°C]	$E_{\text{HOMO}}^c$ [eV]	$E_{\text{LUMO}}^d$ [eV]	$E_g^e$ [eV]
TRZ-MeIAc	409	125	-5.43	-2.46	2.97
NID-MeIAc	379	185	-5.55	-3.10	2.45

<sup>a)</sup> Obtained from TGA measurements. <sup>b)</sup> Obtained from DSC measurements. <sup>c)</sup> Determined by the onset of the oxidation potentials. <sup>d)</sup>  $E_{\text{LUMO}} = E_{\text{HOMO}} + E_g$ . <sup>e)</sup> Estimated from the onset of the absorption spectrum.

## 7. Photophysical properties

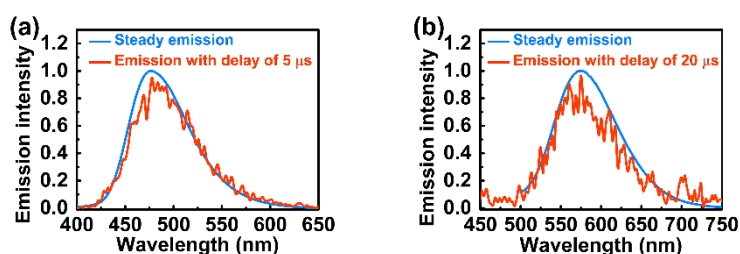


**Figure S10.** (a) Absorption and fluorescence spectra of MeIAC in  $10^{-5}$  M toluene solution at 300 K, and the phosphorescence spectrum of MeIAC in  $10^{-5}$  M toluene solution at 77 K. (b) Cyclic voltammograms of MeIAC in  $\text{CH}_2\text{Cl}_2$ .

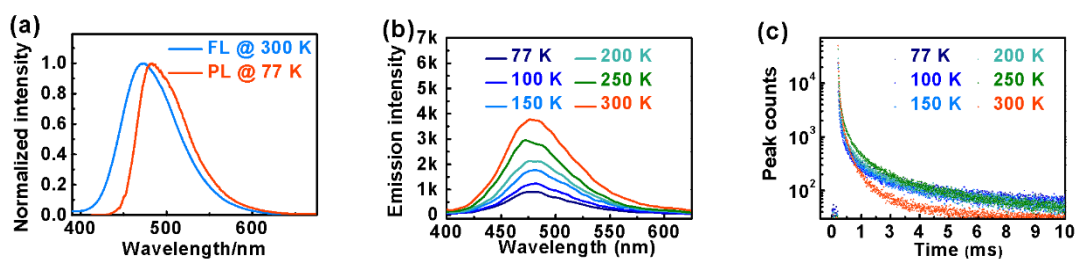
**Table S3.** Photophysical and electrochemical properties of MeIAC.

Compound	$\lambda_{\text{abs}}^{\text{a}}$ [nm]	$\lambda_{\text{fl}}^{\text{a}}$ [nm]	$\lambda_{\text{ph}}^{\text{b}}$ [nm]	$E_{\text{HOMO}}/E_{\text{LUMO}}^{\text{c}}$ [eV]	$E_{\text{g}}^{\text{d}}$ [eV]	$E_{\text{S}}/E_{\text{T}}^{\text{e}}$ [eV]	$\Delta E_{\text{ST}}^{\text{f}}$ [eV]
MeIAC	326	378	439, 469, 498	-5.29/-1.79	3.50	3.52/2.91	0.61

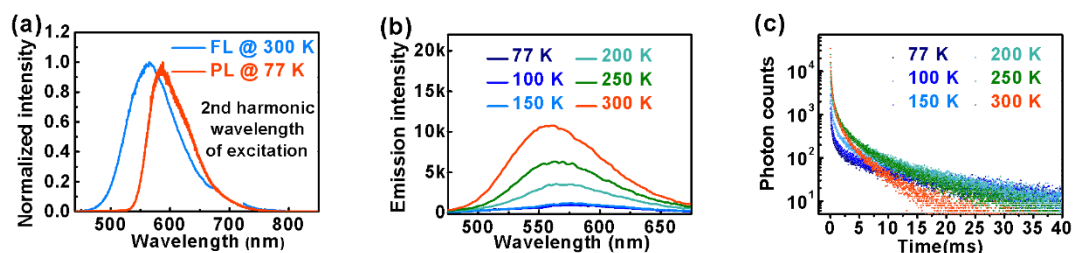
<sup>a)</sup> Measured in toluene solution ( $10^{-5}$  M) at room temperature. <sup>b)</sup> Measured in toluene solution ( $10^{-5}$  M) at 77 K. <sup>c)</sup> The HOMO level was determined by the onset of the oxidation curves, LUMO level was calculated by using HOMO levels and  $E_{\text{g}}$  ( $E_{\text{LUMO}} = E_{\text{HOMO}} + E_{\text{g}}$ ). <sup>d)</sup> Calculated from the edge of the long-wavelength absorption. <sup>e)</sup> Determined by the onset of the fluorescent (300 K) and phosphorescent spectra (77 K) in toluene solution ( $10^{-5}$  M). <sup>f)</sup>  $\Delta E_{\text{ST}} = E_{\text{S}} - E_{\text{T}}$ .



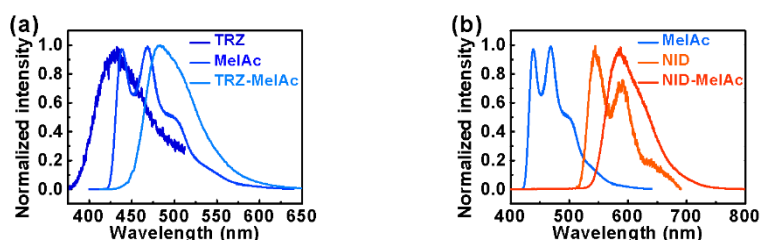
**Figure S11.** (a) The steady and time-resolved photoluminescence spectra of TRZ-MeIAC in  $10^{-5}$  M toluene solution at 300 K. (b) The steady and time-resolved photoluminescence spectra of NID-MeIAC in  $10^{-5}$  M toluene solution at 300 K.



**Figure S12.** (a) The fluorescent (300 K) and phosphorescent spectra (77 K) of 12 wt.% TRZ-MeIAc doped in mCPCN film, (b-c) the steady-state emission and transient photoluminescence decay curves of 12 wt.% TRZ-MeIAc doped in mCPCN film at different temperature.



**Figure S13.** (a) The fluorescent (300 K) and phosphorescent spectra (77 K) of 6 wt.% NID-MeIAc doped in mCPCN film, (b-c) the steady-state emission and transient photoluminescence decay curves of 6 wt.% NID-MeIAc doped in mCPCN film at different temperature.



**Figure S14.** (a) The phosphorescent spectra (77 K) of neat TRZ, neat MeIAc and 12 wt.% TRZ-MeIAc doped in mCPCN film. (b) The phosphorescent spectra (77 K) of neat NID, neat MeIAc and 6 wt.% NID-MeIAc doped in mCPCN film.

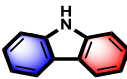
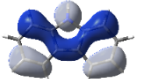
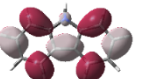
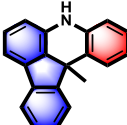
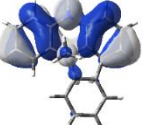
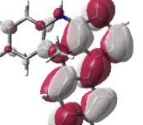
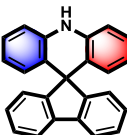

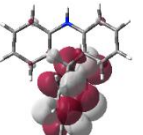
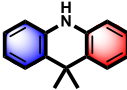

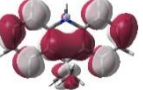
**Table S4.** Photophysical properties of TRZ-MeIAC and NID-MeIAC.

Compound	$\lambda_{\text{abs}}^{\text{a)}$ [nm]	$\lambda_{\text{fl}}^{\text{a)/b)}$ [nm]	$\lambda_{\text{ph}}^{\text{b)}$ [nm]	$E_{\text{S}}/E_{\text{T}}^{\text{c)}$ [eV]	$\Delta E_{\text{ST}}^{\text{d)}$ [eV]	$\tau_{\text{p}}^{\text{a)}$ (ns)	$\tau_{\text{d}}^{\text{a)}$ ( $\mu\text{s}$ )	$\Phi_{\text{Ar}}^{\text{a)}$ (%)	$\Phi_{\text{air}}^{\text{a)}$ (%)	$g_{\text{PL}}^{\text{e)}$ [ $\times 10^{-4}$ ]
TRZ-MeIAC	335, 367	476/473	488	2.93/2.74	0.19	8.6	2.3	49	30	+5.9/-5.9
NID-MeIAC	335, 349, 441	577/565	583	2.50/2.28	0.22	10.5	9.7	6	4	+20/-19

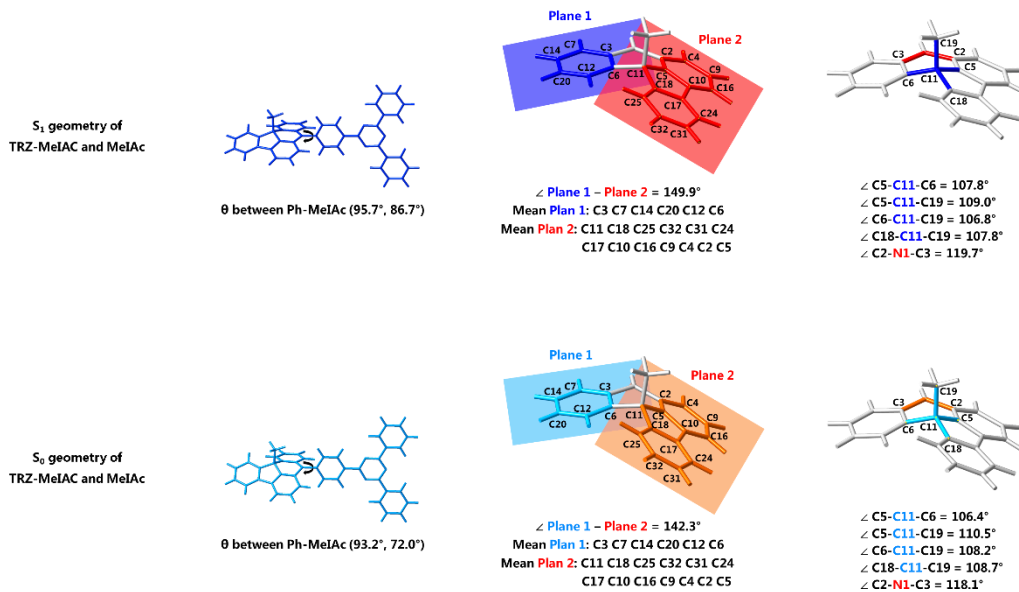
<sup>a)</sup> Measured in toluene solution ( $1.0 \times 10^{-5}$  M) at room temperature. <sup>b)</sup> Measured in doped films with TRZ-MeIAC (12 wt.%) in mCPCN host or NID-MeIAC (6 wt.%) in mCPCN host. <sup>c)</sup> Determined by the onset of the fluorescent spectra (300 K) and phosphorescent spectra (77 K) of the doped films with TADF emitters in mCPCN host. <sup>d)</sup>  $\Delta E_{\text{ST}} = E_{\text{S}} - E_{\text{T}}$ . <sup>e)</sup>  $g_{\text{PL}}$  values of (*R/S*)-TRZ-MeIAC or (*R/S*)-NID-MeIAC enantiomers in toluene solution ( $1.0 \times 10^{-4}$  M) at maximum emission peaks.

## 8. Theoretical simulation

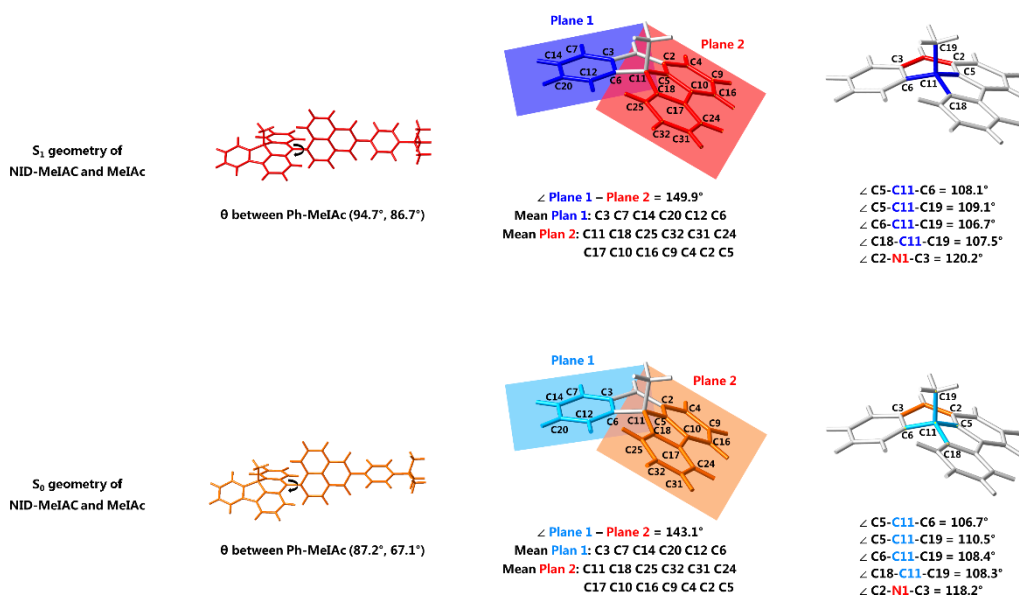
**Table S5.** The calculated results of HOMO and LUMO distribution and levels of Cz, (*R*)-MeIAc, FAc and DMAc by DFT at the B3LYP/def2-SVP level of theory using Gaussian 09.

Compound	Chemical structure	Molecular orbital distribution		$E_{\text{HOMO}}$ [eV]	$E_{\text{LUMO}}$ [eV]	$E_g$ [eV]	Dihedral angle ( $^\circ$ ) <sup>a</sup>
		HOMO	LUMO				
Cz				-5.69	-0.95	4.74	180
( <i>R</i> )-MeIAc				-5.44	-1.06	4.38	141
FAc				-5.28	-1.08	4.20	164
DMAc				-5.12	-0.37	4.75	180

<sup>a</sup>The dihedral angle of the two nitrogen atom linked aromatic units (blue and red filled units in chemical structure).



**Figure S15.** The comparison of optimized structures of S<sub>0</sub> (down) with S<sub>1</sub> state (up) of (R)-TRZ-MeIAC. The optimized structures of MeIAC in (R)-TRZ-MeIAC at S<sub>0</sub> and S<sub>1</sub> state.



**Figure S16.** The comparison of optimized structures of S<sub>0</sub> (down) with S<sub>1</sub> state (up) of (R)-NID-MeIAC. The optimized structures of MeIAC in (R)-NID-MeIAC at S<sub>0</sub> and S<sub>1</sub> state.

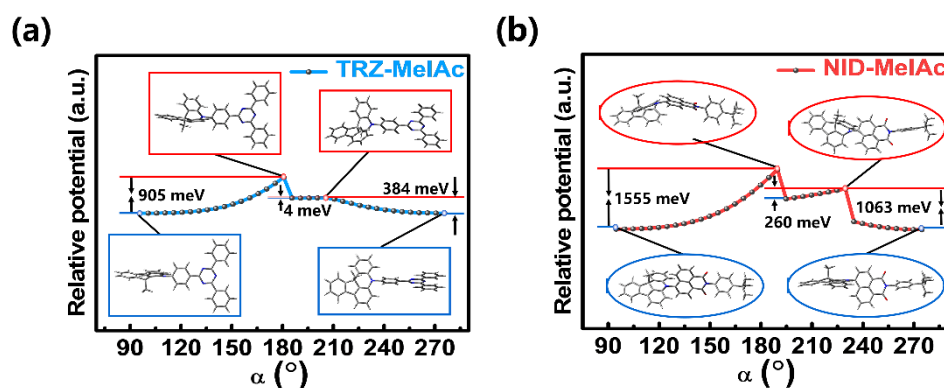
**Table S6.** The calculated potential energy of quasi-equatorial and quasi-axial conformers of (*R*)-TRZ-MeIAc and (*R*)-NID-MeIAc.

Compound	Potential energy (a.u.)			$\Delta E^a)$ (eV)	$E_{AE}^b)$ (eV)	$E_{AA}^c)$ (eV)	$R^d)$ (%)	$\Delta\alpha^e)$ ( $^\circ$ )
	Quasi-equatorial conformer	Quasi-axial conformer	Barrier					
( <i>R</i> )-TRZ-MeIAc	-48899.4446	-48899.3693	-48898.9767	0.0753	0.6074	0.4679	97.4	20
	-48899.4456		-48899.3241	0.0763	0.0452	0.1215		
( <i>R</i> )-NID-MeIAc	-51115.0606	-51114.5767	-51114.2612	0.4839	0.3155	0.7994	> 99.9	10
	-51115.0614		-51114.4619	0.4847	0.1148	0.5995		

<sup>a)</sup> The energy difference between quasi-equatorial and quasi-axial conformer. <sup>b)</sup> The activation energy for quasi-equatorial conformer: the energy difference between the barrier and quasi-axial conformer. <sup>c)</sup> The activation energy for quasi-axial conformer: the energy difference between the barrier and quasi-equatorial conformer. <sup>d)</sup> R: The relative ratios of quasi-equatorial conformer. <sup>e)</sup> The possible molecular rotation angle.

The relative ratios of quasi-equatorial conformer were estimated by Boltzmann distribution<sup>8</sup>:

$$\% \text{ conformer } i = \frac{\exp(-\frac{E_i}{k_b T})}{\sum_j \exp(-\frac{E_j}{k_b T})}$$



**Fig. S17** Flexible potential surface scanning on the energy of the excited singlet state geometry of (*R*)-TRZ-MeIAc (a) and (*R*)-NID-MeIAc (b) at different twisted angles ( $\alpha$ ), the maximized local states and the minimized charge transfer states for (*R*)-TRZ-MeIAc are labeled with red and blue rectangles respectively, the maximized local states and the minimized charge transfer states for (*R*)-NID-MeIAc are labeled with red and blue ellipses, respectively.

## 9. The analysis of the absolute configuration

When the direction of  $\vec{\mu}^{gn}$  is the same as that of  $\vec{m}^{gn}$  (the charge moves along the right-hand spiral path during transition), positive signals in the CPPL spectrum can be found; otherwise, the negative signals present. According to this rule, it can be expected that (*R*)-TRZ-MeIAc with same directional  $\vec{\mu}^{gn}$  and  $\vec{m}^{gn}$  (the vector angle  $\theta_{\mu,m}$  of 14.5 °) should demonstrate positive signals in CPPL spectra. The experimental results (**Figure 2b,c** in main text, **Figure S1-S2**) for (***R***)-**TRZ-MeIAc** (the obtained Peak 1 during the chiral HPLC resolution, the absolute configuration was confirmed by the single crystal) matched well with the theoretical prediction (**Table 2** in main text). And the same trend was also found in the simulations and experimental results of (*S*)-TRZ-MeIAc (**Figure 2b,c**, **Table 2**, **Figure S3-S4**).

Based on the above results, the absolute configuration of the enantiomers of NID-MeIAc could be confirmed. According to the simulated same dipole moment direction in (*R*)-NID-MeIAc (**Table 2**), the obtained Peak 1 during the chiral HPLC resolution with positive CPPL signals can be considered to be *R* configuration and the obtained Peak 2 can be considered to be *S* configuration (**Figure 2e,f** in main text, **Figure S3-S4**).

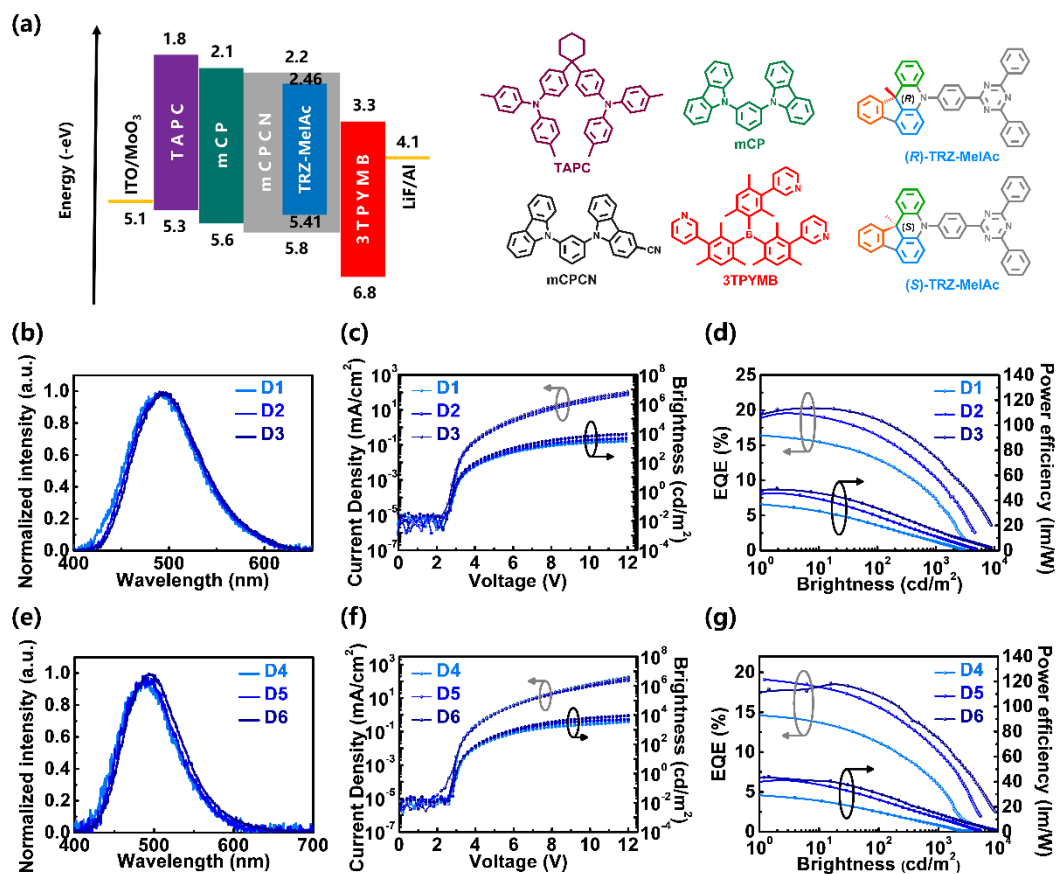


## 10. Supplemental electroluminescence data

**Table S7.** The summary of EL characteristics for OLED structures of: ITO/MoO<sub>3</sub> (1 nm)/TAPC (45 nm)/mCP (10 nm)/mCPCN: *x* wt.% (*R*)-TRZ-MeIAc or (*S*)-TRZ-MeIAc (20 nm)/3TPYMB (50 nm)/LiF/Al.

Emitter	Device	V <sub>on</sub> <sup>a)</sup> [V]	EL <sub>peak</sub> <sup>b)</sup> [nm]	CE <sup>c)</sup> [cd·A <sup>-1</sup> ]	PE <sup>d)</sup> [lm·W <sup>-1</sup> ]	EQE <sup>e)</sup> [%]
<i>(R)</i> -TRZ-MeIAc	D1 (4 wt.%)	3.0	490	36.2	38.0	16.6
	D2 (8 wt.%)	3.0	490	45.3	47.6	19.8
	D3 (12 wt.%)	2.9	494	47.8	49.6	20.3
<i>(S)</i> -TRZ-MeIAc	D4 (4 wt.%)	3.0	487	28.8	30.1	14.8
	D5 (8 wt.%)	3.0	490	41.6	43.6	19.1
	D6 (12 wt.%)	2.9	494	42.1	44.1	18.7

<sup>a)</sup> The turn-on voltage recorded at a brightness of 1 cd·m<sup>-2</sup>. <sup>b)</sup> The peak wavelength of the EL spectrum. The maximum value of <sup>c)</sup> current efficiency; <sup>d)</sup> power efficiency; <sup>e)</sup> external quantum efficiency.

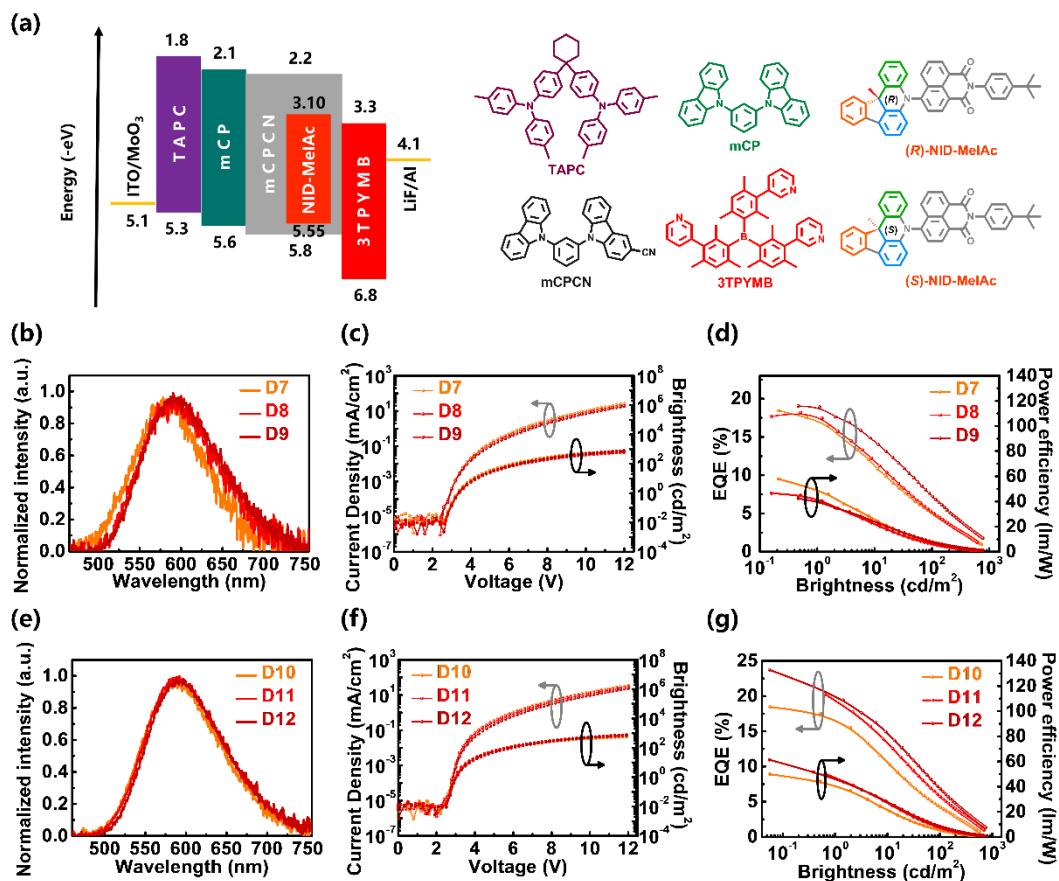


**Figure S18.** (a) The device structure, energy level diagram, and the molecular structures of the materials employed in the devices. (b-g) Electroluminescence spectra, luminance-voltage-current density characteristics, external quantum efficiency and power efficiency characteristics for devices based on (*R*)-TRZ-MeIac (D1 to D3) and (*S*)-TRZ-MeIac (D4 to D6).

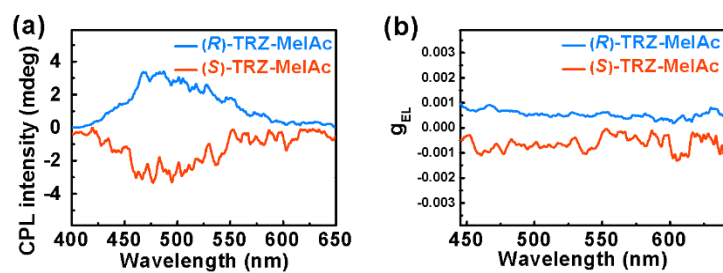
**Table S8.** The summary of EL characteristics for OLED structures of: ITO/MoO<sub>3</sub> (1 nm)/TAPC (70 nm)/mCP (10 nm)/mCPCN: x wt.% (*R*)-NID-MeIAc or (*S*)-NID-MeIAc (20 nm)/3TPYMB (70 nm)/LiF/Al.

Emitter	Device	V <sub>on</sub> <sup>a)</sup> [V]	EL <sub>peak</sub> <sup>b)</sup> [nm]	CE <sup>c)</sup> [cd·A <sup>-1</sup> ]	PE <sup>d)</sup> [lm·W <sup>-1</sup> ]	EQE <sup>e)</sup> [%]
	D7 (1.5 wt.%)	3.1	581	71.2	57.8	18.4
<i>(R)</i> -NID-MeIAc	D8 (3 wt.%)	3.1	591	72.2	46.6	18.2
	D9 (6 wt.%)	3.1	591	74.5	42.3	19.0
	D10 (1.5 wt.%)	3.1	583	44.4	49.8	18.5
<i>(S)</i> -NID-MeIAc	D11 (3 wt.%)	3.1	589	72.6	50.2	20.3
	D12 (6 wt.%)	3.1	589	68.4	61.3	23.7

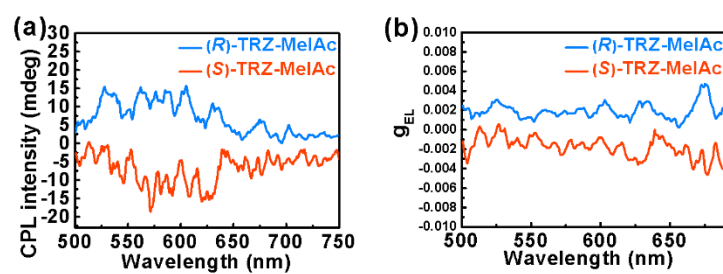
<sup>a)</sup> The turn-on voltage recorded at a brightness of 1 cd·m<sup>-2</sup>. <sup>b)</sup> The peak wavelength of the EL spectrum. The maximum value of <sup>c)</sup> current efficiency; <sup>d)</sup> power efficiency; <sup>e)</sup> external quantum efficiency.



**Figure S19.** (a) The device structure, energy level diagram, and the molecular structures of the materials employed in the devices. (b-g) Electroluminescence spectra, luminance-voltage-current density characteristics, external quantum efficiency and power efficiency characteristics for devices based on (*R*)-NID-MeIAC (D7 to D9) and (*S*)-NID-MeIAC (D10 to D12).

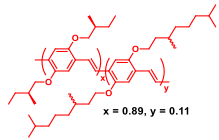
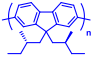
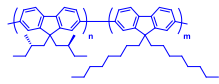
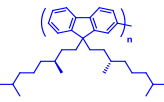
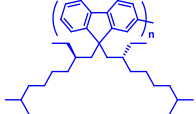
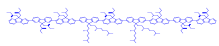
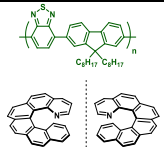
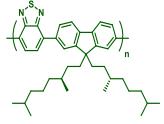
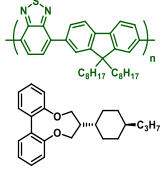
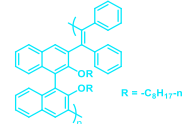


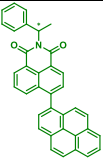
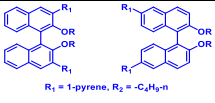
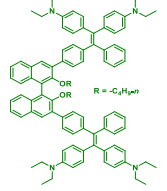
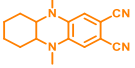
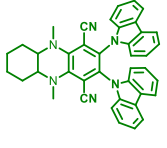
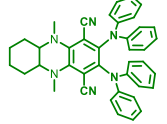
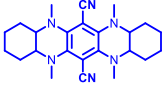
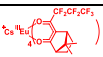
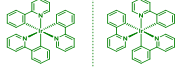
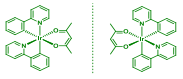
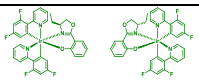
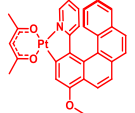
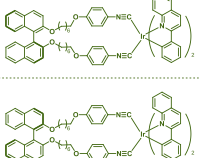
**Figure S20.** CPEL spectra (a) and  $g_{EL}$  of (R/S)-TRZ-MeIAc (b) in device D3/D6.



**Figure S21.** CPEL spectra (a) and  $g_{EL}$  of (R/S)-NID-MeIAc (b) in device D9/D12.

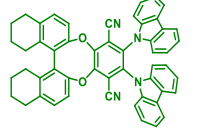
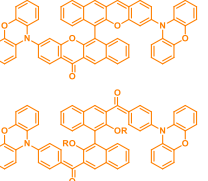
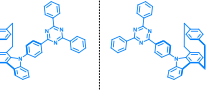
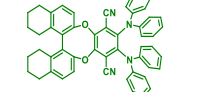
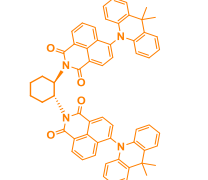

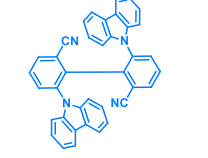
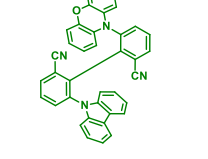
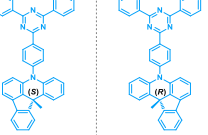
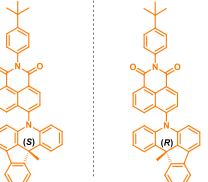
**Table S9.** The device performances of reported CP-OLEDs vs this work.

Materials	Structure	Device models	Type of emitters	EL <sub>peak</sub> [nm]	L <sub>max</sub> [cd m <sup>-2</sup> ]	CE <sub>max</sub> [cd A <sup>-1</sup> ]	PE <sub>max</sub> [lm W <sup>-1</sup> ]	EQE <sub>max</sub> [%]	g <sub>EL</sub>	Ref.
PPV-co-BDMO-PPV		Pure polymer layer	Common fluorescent material	600	-	-	-	-	-1.7 × 10 <sup>-3</sup>	[11]
(S)-PF4/1		Pure polymer layer	Common fluorescent material	425/512	-	-	-	-	+0.16	[12]
(S)-PF4/1-co-PF8		Pure polymer layer	Common fluorescent material		-	-	-	-	+0.05	
(S)-PF8/1/1		Pure polymer layer	Common fluorescent material		-	-	-	-	-0.25	
(R)-PF2/6		Pure polymer layer	Common fluorescent material		-	-	-	-	-0.25	
C-522		Pure oligomer layer	Common fluorescent material	425/450	-	0.94	-	-	+0.35	[13]
F8BT/1-aza[6]helicene		F8BT with chiral dopant	Common fluorescent material	540	3000	-	1.1	-	-0.2/ +0.2	[14]
c-PFBT		Pure polymer layer	Common fluorescent material	510	80	-	0.12	-	-0.8	[15]
F8BT/R5011		F8BT Dispersed in R5011	Common fluorescent material	546	4000	4.46	-	-	-1.13	[16]
S/R-P		Pure polymer layer	Common fluorescent material	505	1669/ 1270	0.926/ 0.833	0.390/ 0.422	-	+0.024/ -0.019	[17]

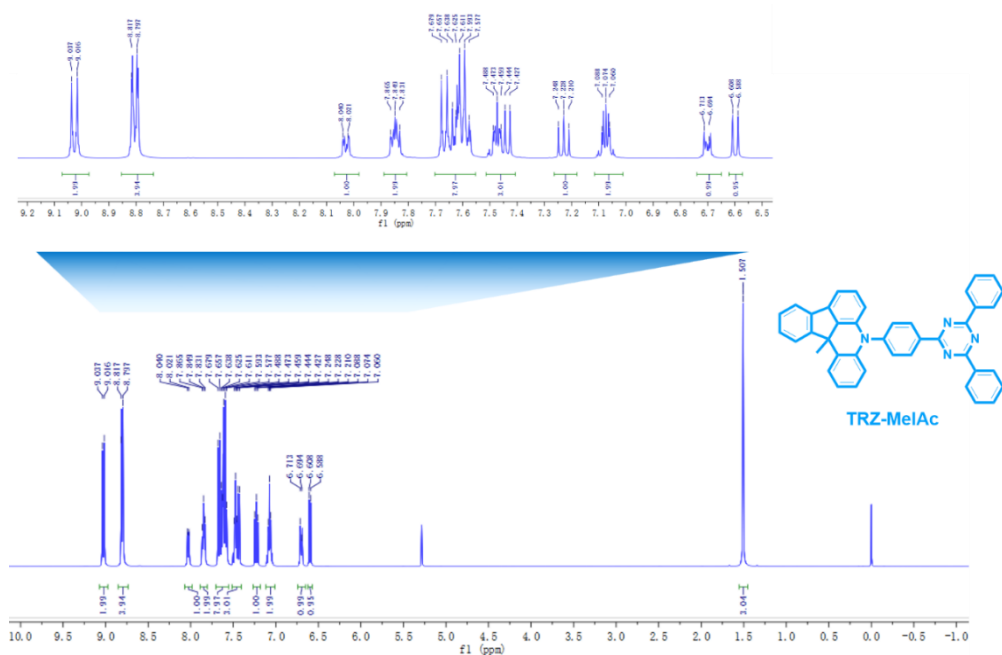
S/R-2		Pure small molecular layer	Common fluorescent material	520	19575/18411	2.8/3.2	-	1.0/1.1	+0.0022/-0.0022	[18]
R/S-5 R/S-6	 R <sub>1</sub> = 1-pyrene, R <sub>2</sub> = -C <sub>6</sub> H <sub>4</sub> -n	Pure small molecular layer	Common fluorescent material	460/ 480	11336/10886/ 24806/ 22880	3.91/ 3.86/ 5.17/ 4.26	-	2.79/ 2.17/ 3.09/ 2.27	+0.0056/ -0.0052/ +0.00078/ -0.00074/	[19]
S/R-6	 R = -C <sub>6</sub> H <sub>4</sub> -m	Pure small molecular layer	Common fluorescent material	534	8061/ 7946	1.32/ 1.26	-	0.48/ 0.45	+0.0036/ -0.0032/	[20]
BA		Dispersed in 26DCzPPy	Common fluorescent material	593	7145	5.12	3.4	2.0	+0.00045/ -0.0005	[21]
DCz				508	22956	17.6	11.2	5.5	+0.00077/ -0.00083	
DPA				540	13426	9.7	6.4	2.5	+0.00057/ -0.00078	
PT				420	1936	0.91	0.4	1.7	+0.0013/ -0.0014	
CsEu(hfbc) <sub>4</sub>		Dispersed in PVK and OXD7	Lanthanide complexes	595, 612	-	-	-	0.05	-1.00 to +0.19	[22]
Δ-fac-Ir(ppy) <sub>3</sub> / Δ-fac-Ir(ppy) <sub>3</sub>		Dispersed in mCP	Phosphorescent Iridium complexes	522/ 515	-	-	-	-	-0.00028/ +0.00068	[23]
Δ-fac-Ir(ppy) <sub>2</sub> acac/ Δ-fac-Ir(ppy) <sub>2</sub> acac				533/ 509					-0.00031/ +0.0043	
Δ-Ir(dppy) <sub>2</sub> (R-edp)/ Δ-Ir(dppy) <sub>2</sub> (R-edp)				514/ 510					-0.0026/ +0.00049/	
1		Dispersed in PVK and OXD7	Phosphorescent Platinum complexes	615	222	0.25	0.11	-	-0.38	[24]
SI/R1		Dispersed in PVK and OXD7	Phosphorescent Iridium complexes	526/ 558	4257	7.50	2.44	-	up to 10 <sup>-3</sup>	[25]

(P/M)-Pt		Dispersed in TCTA and 26DCzPPy	Phosphorescent Platinum complexes	~650	9732/11590	19.52/22.52	15.39/18.62	16.29/18.81	-0.0016/ +0.0014 to -0.0037/ +0.0051	[26]
$\Delta$ -(tfpqz) <sub>2</sub> Ir(R-L2)/ $\Lambda$ -(tfpqz) <sub>2</sub> Ir(S-L2)		Dispersed in 26DCzPPy	Phosphorescent Iridium complexes	595/599	34986/44745	54.6/54.4	51.3/52.1	23.7/23.6	+0.0005/ -0.0003	[27]
[Pt(iqbt)(S-L <sup>o</sup> )(1-4)]		Dispersed in PVK-PBD	Phosphorescent Platinum complexes	732	-	-	-	up to 0.93	up to 0.0027	[28]
BP1		Dispersed in CBP	Phosphorescent Platinum complexes	600, 650, 715	1062/1018	1.43/1.52	0.90/0.80	1.32/1.49	+0.0012/ -0.0007	[29]
BP2				600, 650, 715	3500/3318	2.83/2.64	1.38/1.28	2.15/2.01	+0.0011/ -0.0010	
(P/M)-SD		Dispersed in 26DCzPPy	Phosphorescent Platinum complexes	653	2156/1927	2.32/2.26	1.97/2.03	4.60/4.42	+0.0013/ -0.0011	[30]
R/S-ZnL		Pure small molecular layer	Zn(II) Complex	576	860/1000	0.18/0.19	0.071/0.085	0.038/0.042	+0.015/ -0.015	[31]
(R/S)-1		Dispersed in mCP	TADF emitter	-	-	34.7	16.3	9.1	-	[32]
(R,R/S,S)-CAI-Cz		Dispersed in mCBP	TADF emitter	520	-	59.4/59.0	52.9/53.0	19.8/19.7	+0.0023/ -0.0017	[33]
R/S-BN-CF, R/S-BN-CCB, R/S-BN-DCB, and R/S-BN-AF		Dispersed in mCP	TADF emitter	496-597	1473-6633	1.1-24.6	0.7-19.6	0.6-9.3	-0.091 to +0.084	[34]

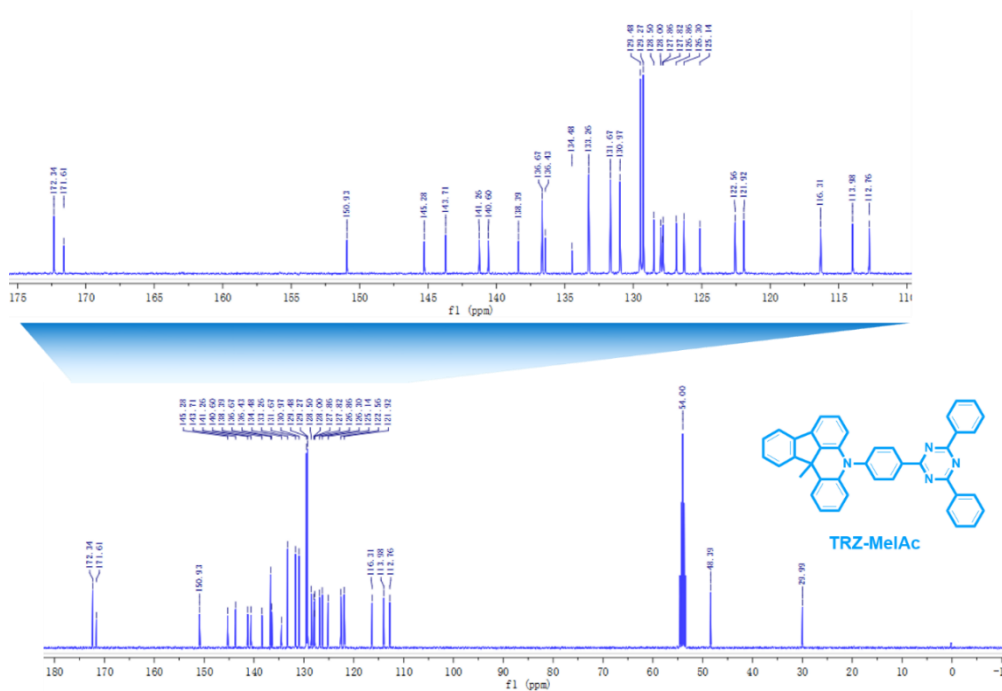


( <i>R/S</i> )-OBN-Cz		Dispersed in 26DCzPPy or pure small molecular layer	TADF emitter	501/526	46651 / 35633	93.7/47.8	59.7/34.6	32.6/14.0	+0.00228/ -0.00234	[35]
<i>R/S</i> -1		Dispersed in TCTA or pure small molecular layer	TADF emitter	580-604	2726-11783	0.22-4.2	-	0.12-1.8	-0.0009 to +0.001	[36]
CzPhTrz		Dispersed in mCP	TADF emitter	480	-	34.8	32.5	17.0	-	[37]
( <i>R/S</i> )-OBN-DPA		Dispersed in TCTA or pure small molecular layer	TADF emitter	544/560	15161 - 25418	22.7-45.3	15.8-30.7	6.6-12.3	-0.0022 to +0.0029	[38]
(-)-( <i>R,R</i> )-CAI-DMAC/ (+)-( <i>S,S</i> )-CAI-DMAC		Dispersed in CBP	TADF emitter	592	-	28.8/28.5	26.6/28.0	12.3/12.4	-	[39]
<i>S/R</i> -CPDCz, <i>S/R</i> -CPDCB	 R = H or <i>t</i> -Bu	Dispersed in mCP	TADF emitter	492-518	923-7700	21.4-39.5	15.7-30.3	8.4-12.4	-0.0039 to +0.0035	[40]
<i>S/R</i> -Cz-Ax-CN		Dispersed in DPEPO	TADF emitter	468	-	20.9	16.4	12.7	-0.012/ +0.014	[41]
<i>S/R</i> -BPPOACZ		Dispersed in 2,6-DCzPPy	TADF emitter	537	38128	61.0	42.6	17.8	+0.0045/ -0.0028	[42]
( <i>R/S</i> )-TRZ-MeIac		Dispersed in mCPCN	TADF emitter	494	8796/9074	47.8/42.1	49.6/44.1	20.3/18.7	+0.00071/ -0.00084	This work
( <i>R/S</i> )-NID-MeIac		Dispersed in mCPCN	TADF emitter	591	772/750	74.5/68.4	42.3/61.3	19.0/23.7	+0.0020/ -0.0024	

## 11. $^1\text{H}$ NMR, $^{13}\text{C}$ NMR and HRMS spectroscopies



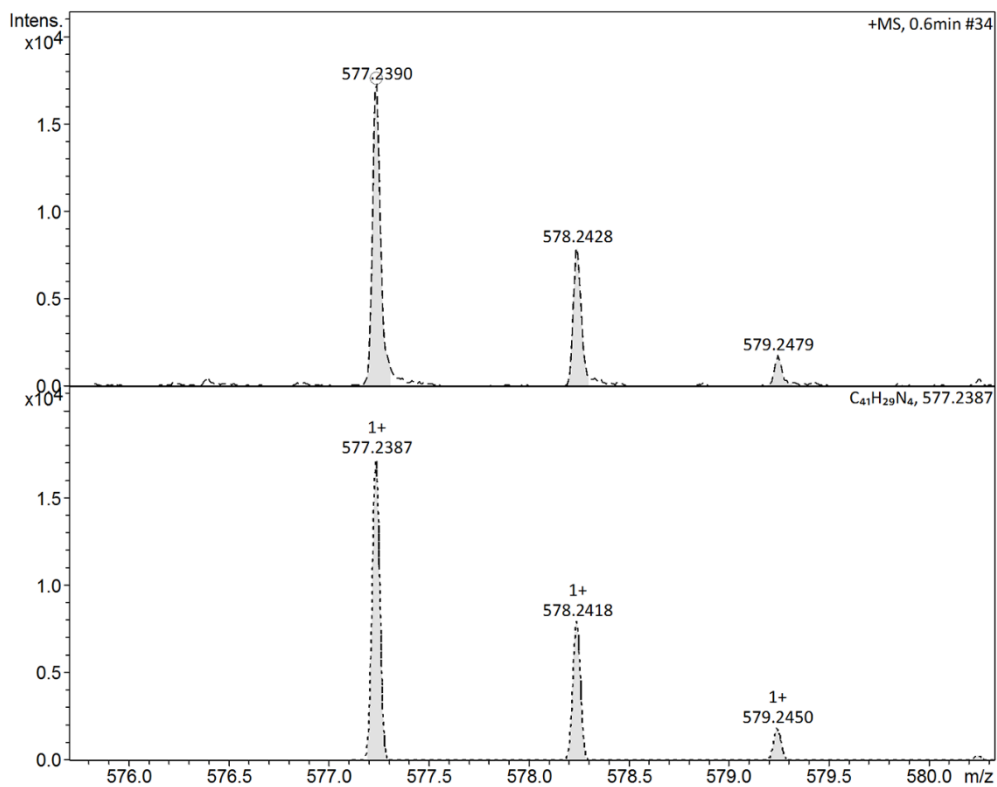
$^1\text{H}$  NMR spectroscopies for TRZ-MeAc



$^{13}\text{C}$  NMR spectroscopies for TRZ-MeAc

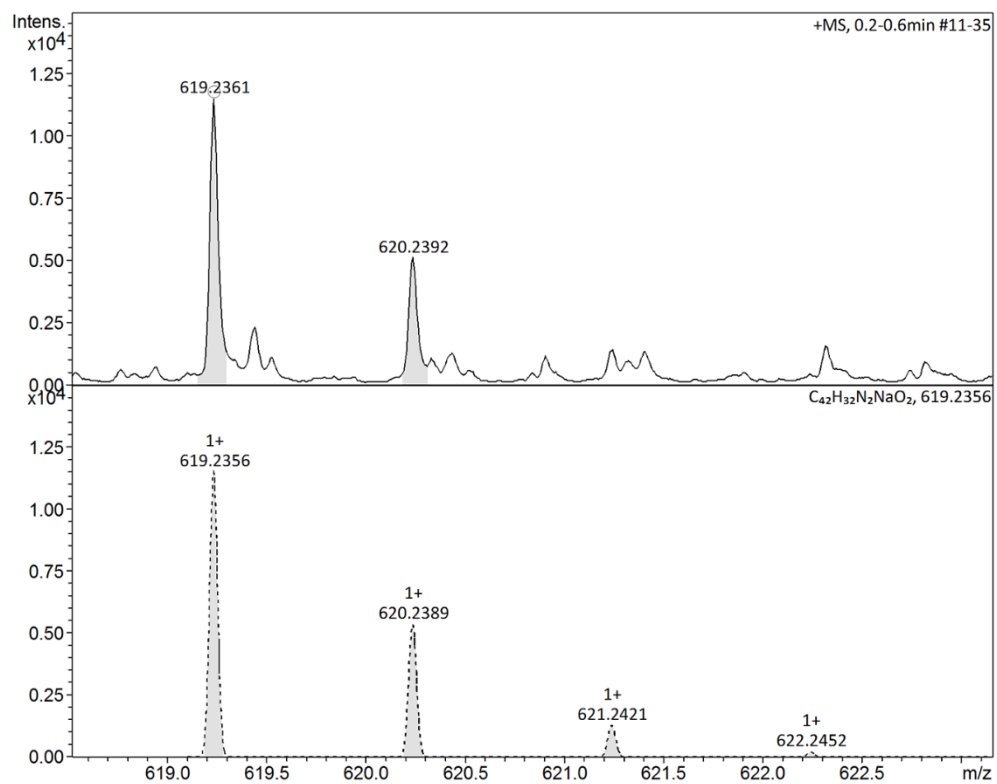


**+MS, 0.6min #34**



HRMS for TRZ-MeIac

**+MS, 0.2-0.6min #11-35**



HRMS for NID-MeIac

## 12. References

- (1) S. Grimmea, J. Antony, S. Ehrlich, H. Krieg, *J. Chem. Phys.* **2010**, *132*, 154104.
- (2) T. Lu, F. Chen, *J. Comput. Chem.* **2012**, *33*, 580.
- (3) W. Zeng, S. Gong, C. Zhong, C. Yang, *J. Phys. Chem. C* **2019**, *123*, 10081.
- (4) H. Tanaka, Y. Kato, M. Fujiki, Y. Inoue, T. Mori, *J. Phys. Chem. A* **2018**, *122*, 7378.
- (5) K. C. Pan, S. W. Li, Y. Y. Ho, Y. J. Shiu, W. L. Tsai, M. Jiao, W. K. Lee, C. C. Wu, C. L. Chung, T. Chatterjee, *Adv. Funct. Mater.* **2016**, *26*, 7560.
- (6) N. Berova, P. L. Polavarapu, K. Nakanishi, R. W. Woody, *Comprehensive Chiroptical Spectroscopy, Volume 1: Instrumentation, Methodologies, and Theoretical Simulations*, First Edition. Wiley, Hoboken, NJ, USA **2012**.
- (7) a) R. C. Hilborn, *Am. J. Phys.* **1982**, *50*, 982; b) M. Uejima, T. Sato, D. Yokoyama, K. Tanaka, J.-W. Park, *Phys. Chem. Chem. Phys.* **2014**, *16*, 14244; c) X. Mu, X. Chen, J. Wang, M. Sun, *J. Phys. Chem. A* **2019**, *123*, 8071.
- (8) a) Y. Olivier, M. Moral, L. Mucciolicd, J.-C. Sancho-Garc á, *J. Mater. Chem. C* **2017**, *5*, 5718; b) K. Wang, C. Zheng, W. Liu, K. Liang, Y. Shi, S. Tao, C. Lee, X. Ou, X. Zhang, *Adv. Mater.* **2017**, *29*, 1701476; c) W. Li, X. Cai, B. Li, L. Gan, Y. He, K. Liu, D. Chen, Y. Wu, S. Su, *Angew. Chem. Int. Ed.* **2019**, *58*, 582.
- (9) H. D. Flack, *Acta Cryst.* **1983**, *A39*, 876.
- (10) B. Kim, G. Storch, G. Banerjee, B. Q. Mercado, J. Castillo-Lora, G. W. Brudvig, J. M. Mayer, S. J. Miller, *J. Am. Chem. Soc.* **2017**, *139*, 15239.
- (11) E. Peeters, M. P. T. Christiaans, R. A. J. Janssen, H. F. M. Schoo, H. P. J. M. Dekkers, E. W. Meijer, *J. Am. Chem. Soc.* **1997**, *119*, 9909.
- (12) a) M. Oda, H. Nothofer, G. Lieser, U. Scherf, S. C. J. Meskers, D. Neher, *Adv. Mater.* **2000**, *12*, 362; b) M. Oda, H. Nothofer, U. Scherf, V. Šunjić, D. Richter, W. Regenstein, D. Neher, *Macromolecules* **2002**, *35*, 6792.
- (13) Y. Geng, A. Trajkovska, S. W. Culligan, J. J. Ou, H. M. P. Chen, D. Katsis, S. H. Chen, *J. Am. Chem. Soc.* **2003**, *125*, 14032.
- (14) Y. Yang, R. C. Costa, D.-M. Smilgies, A. J. Campbell, M. J. Fuchter, *Adv. Mater.* **2013**, *25*, 2624.
- (15) D. D. Nuzzo, C. Kulkarni, B. Zhao, E. Smolinsky, F. Tassinari, S. C. J. Meskers, R. Naaman, E. W. Meijer, R. H. Friend, *ACS Nano* **2017**, *11*, 12713.
- (16) a) D. Lee, J. Song, Y. Lee, C. Yu, J. Kim, *Adv. Mater.* **2017**, *29*, 1700907; b) J. Jung, D. Lee, J. Kim, C. Yu, *J. Mater. Chem. C* **2018**, *6*, 726.
- (17) L. Yang, Y. Zhang, X. Zhang, N. Li, Y. Quan, Y. Cheng, *Chem. Commun.* **2018**, *54*, 9663.

- (18) Y. Zhang, X. Zhang, H. Zhang, Y. Xiao, Y. Quan, S. Ye, Y. Cheng, *J. Phys. Chem. C* **2019**, *123*, 24746.
- (19) X. Zhang, Y. Zhang, Y. Li, Y. Quan, Y. Cheng, Y. Li, *Chem. Commun.* **2019**, *55*, 9845.
- (20) X. Zhang, Y. Zhang, H. Zhang, Y. Quan, Y. Li, Y. Cheng, S. Ye, *Org. Lett.* **2019**, *21*, 439.
- (21) X. Luo, H. Han, Z. Yan, Z. Wu, J. Su, J. Zou, Z. Zhu, Y. Zheng, J. Zuo, *ACS Appl. Mater. Interfaces* **2020**, *20*, 23172.
- (22) a) F. Zinna, U. Giovanella, L. D. Bari, *Adv. Mater.* **2015**, *27*, 1791; b) F. Zinna, M. Pasini, F. Galeotti, C. Botta, L. D. Bari, U. Giovanella, *Adv. Funct. Mater.* **2017**, *27*, 1603719.
- (23) T. Li, Y. Jing, X. Liu, Y. Zhao, L. Shi, Z. Tang, Y. Zheng, J. Zuo, *Sci. Rep.* **2015**, *5*, 14912.
- (24) J. R. Brandt, X. Wang, Y. Yang, A. J. Campbell, M. J. Fuchter, *J. Am. Chem. Soc.* **2016**, *138*, 9743.
- (25) J. Han, S. Guo, J. Wang, L. Wei, Y. Zhuang, S. Liu, Q. Zhao, X. Zhang, W. Huang, *Adv. Optical Mater.* **2017**, *5*, 1700359.
- (26) Z. Yan, X. Luo, W. Liu, Z. Wu, X. Liang, K. Liao, Y. Wang, Y. Zheng, L. Zhou, J. Zuo, Y. Pan, H. Zhang, *Chem. Eur. J.* **2019**, *25*, 5672.
- (27) Z. Yan, K. Liao, H. Han, J. Su, Y. Zheng, J. Zuo, *Chem. Commun.* **2019**, *55*, 8215.
- (28) G. Fu, Y. He, W. Li, B. Wang, X. Lü, H. He, W. Y. Wong, *J. Mater. Chem. C* **2019**, *7*, 13743.
- (29) Z. Jiang, J. Wang, T. Gao, J. Ma, Z. Liu, R. Chen, *ACS Appl. Mater. Interfaces* **2020**, *12*, 9520.
- (30) Z. Yan, X. Luo, K. Liao, Y. Zheng, J. Zuo, *Front. Chem.* **2020**, *8*, 501.
- (31) Y. Chen, X. Li, N. Li, Y. Quan, Y. Cheng, Y. Tang, *Mater. Chem. Front.* **2019**, *3*, 867.
- (32) S. Feuillastre, M. Pauton, L. Gao, A. Desmarchelier, A. J. Riives, D. Prim, D. Tondelier, B. Geffroy, G. Muller, G. Clavier, G. Pieters, *J. Am. Chem. Soc.* **2016**, *138*, 3990.
- (33) M. Li, S. Li, D. Zhang, M. Cai, L. Duan, M. Fung, C. Chen, *Angew. Chem. Int. Ed.* **2018**, *57*, 2889.
- (34) F. Song, Z. Xu, Q. Zhang, Z. Zhao, H. Zhang, W. Zhao, Z. Qiu, C. Qi, H. Zhang, H. H. Y. Sung, I. D. Williams, J. W. Y. Lam, Z. Zhao, A. Qin, D. Ma, B. Z. Tang, *Adv. Funct. Mater.* **2018**, *28*, 1800051.
- (35) Z. Wu, H. Han, Z. Yan, X. Luo, Y. Wang, Y. Zheng, J. Zuo, Y. Pan, *Adv. Mater.* **2019**, *31*, 1900524.
- (36) Y. Wang, Y. Zhang, W. Hu, Y. Quan, Y. Li, Y. Cheng, *ACS Appl. Mater. Interfaces* **2019**, *11*, 26165.

- (37) N. Sharma, E. Spuling, C. M. Mattern, W. Li, O. Fuhr, Y. Tsuchiya, C. Adachi, S. Br äse, I. D. W. Samuel, E. Zysman-Colman, *Chem. Sci.* **2019**, *10*, 6689.
- (38) Z. Wu, Z. Yan, X. Luo, L. Yuan, W. Liang, Y. Wang, Y. Zheng, J. Zuo, Y. Pan, *J. Mater. Chem. C* **2019**, *7*, 7045.
- (39) Y. Wang, H. Lu, C. Chen, M. Li, C. Chen, *Org. Electron.* **2019**, *70*, 71.
- (40) . Sun, J. Wang, L. Chen, R. Chen, J. Jin, C. Chen, S. Chen, G. Xie, C. Zheng, W. Huang, *J. Mater. Chem. C* **2019**, *7*, 14511.
- (41) M. Li, Y. Wang, D. Zhang, L. Duan, C. Chen, *Angew. Chem. Int. Ed.* **2020**, *59*, 3500.
- (42) Z. Tu, Z. Yan, X.Liang, L. Chen, Zh. Wu, Y. Wang, Y. Zheng, J. Zuo, Y. Pan, *Adv. Sci.* **2020**, *7*, 2000804.
- (43) L. Fr é d éric, A. Desmarchelier, R. Plais, L. Lavnevich, G. Muller, C. Villafuerte, G. Clavier, E. Quesnel, B. Racine, S. Meunier-Della-Gatta, J.-P. Dognon, P. Thu éry, J. Crassous, L. Favereau, G. Pieters, *Adv. Funct. Mater.* **2020**, *30*, 2004838.